

Radio streaks in the Lighthouse Nebula discovered with MeerKAT

Particles escaping from the tail and illuminating the ambient magnetic field

Pierrick Martin¹*, Mickael Coriat¹, Barbara Olmi², Elena Amato^{2,3},
Niccolò Bucciantini^{2,3,4}, Alexandre Marcowith⁵, and Sarah Recchia^{6,2}

¹ IRAP, Université de Toulouse, CNRS, CNES, F-31028 Toulouse, France

² Osservatorio Astrofisico di Arcetri, INAF, Largo Enrico Fermi 5 I-50125, Firenze, Italy

³ Università degli Studi di Firenze, Via Sansone 1 I-50019, Sesto F.ino (FI), Italy

⁴ INFN , Sezione di Firenze, Via G. Sansone 1, I-50019 Sesto Fiorentino (FI), Italy

⁵ LUPM, Université de Montpellier, CNRS/IN2P3, CC72, Place Eugène Bataillon, F-34095, France

⁶ IFJ-PAN, Institute of Nuclear Physics Polish Academy of Sciences, PL-31342 Krakow, Poland

Received XXX; accepted YYY

ABSTRACT

Context. Bow-shock pulsar wind nebulae are valuable sources to investigate the dynamics of relativistic pulsar winds and the mechanisms by which they are converted into cosmic-ray leptons at the highest energies. The Lighthouse Nebula is one such object, famous for the high velocity of its pulsar and a long misaligned X-ray jet that is understood as a specific escape channel for the most energetic particles.

Aims. We aim to get a better understanding of how the bulk of non-thermal particles are released into the interstellar medium. We focus on GHz radio observations, which probe lower-energy particles that are dominant in number and long-lived, thus offering a picture of how escape proceeds in the long run.

Methods. We analyze 10.5 h of MeerKAT observations in the 0.9 – 1.7 GHz band.

Results. MeerKAT observations reveal a highly structured synchrotron nebula downstream of pulsar PSR J1101-6101. A cometary tail is detected up to beyond 5pc from the pulsar, while a system of multiple transverse two-sided emission streaks is observed for the first time. No radio counterpart of the misaligned X-ray jet is seen.

Conclusions. The radio streaks are interpreted as the occasional charge-independent release of energetic leptons from the tail into the surrounding medium, as a result of dynamical instabilities and reconfiguration in the downstream flow. The intensity layout suggests that most of the particle content of the nebula is discharged into the ambient medium within several parsec. Once escaped, particles light up the ambient magnetic field, which appears to have a coherence length of at least a few parsec. The length and persistence of the streaks indicate a low level of magnetic turbulence, possibly slightly enhanced with respect to average cosmic-ray transport conditions in the Galaxy. Such a confinement may result from self-generated turbulence by resonant streaming instability, or be due to past activity of the progenitor star.

Key words. pulsars:general – Acceleration of particles – ISM: magnetic fields – (ISM:) cosmic rays

1. Introduction

Pulsars, rapidly spinning and highly magnetized neutron stars created in most core-collapse supernovae, store about 10^{48} – 10^{49} erg of rotational energy that they return to their surroundings in 10^2 – 10^5 yr time scales. Pulsars release their energy by producing a cold and magnetized pair-plasma outflow with Lorentz factors 10^4 – 10^7 (the presence of ions in this wind is still debated). The interaction of this ultra-relativistic wind with the surrounding medium generates a shock where the kinetic energy of the wind is converted into non-thermal particles. Although not yet fully elucidated, the process is inferred to be very efficient (with conversion rates ~10-100%) and to produce very extended particle distributions (ranging from GeV to PeV). The structure forming downstream of the wind termination shock (TS), up to the contact discontinuity (CD) separating shocked pulsar wind and stellar ejecta, is called a pulsar wind nebula (PWN). It is essentially composed of non-thermal electron-positron pairs bathed in a strong and turbulent magnetic

field. As a result, PWNe shine over the entire electromagnetic spectrum via the production of intense synchrotron and inverse-Compton scattering radiation and constitute a prominent class of Galactic sources especially in the radio, X-ray, and gamma-ray domain. Recent reviews on PWNe can be found in Mitchell & Gelfand (2022); Olmi (2023); Olmi & Bucciantini (2023).

In its early evolution ($t \lesssim 10^3$ yr), the PWN is fed by a maximally powerful pulsar and it grows fast in a cold stellar ejecta ($R_{\text{PWN}} \propto t^{6/5}$; van der Swaluw et al. 2001). At intermediate ages ($10^4 \lesssim t \lesssim 10^5$ yr) the PWN evolution is instead determined by its interaction with the reverse shock (RS) of the supernova remnant (SNR), an inverse shock moving from the ejecta outer boundary towards the center of the stellar explosion, compressing and heating the stellar ejecta. The PWN ends up confined in high-pressure medium and, depending on its energetic reservoir, it might compress and re-expand under the pressure exerted by the shocked ejecta (one-zone models actually predict multiple cycles of compressions-expansions that are likely suppressed in three dimensions, see e.g. Bandiera et al. 2023 and the references therein), modifying its morphology and spectral properties. The

* pierrick.martin@irap.omp.eu

PWN growth is shallower at late times ($R_{\text{PWN}} \propto t^{3/10}$; van der Swaluw et al. 2001). In this stage, the pulsar can escape the PWN and then the SNR as a result of the initial impulse it received in the supernova explosion. The typical velocities inferred from the observed proper motions are in the $100 - 1000 \text{ km s}^{-1}$ range (Verbiest et al. 2017; Igoshev 2020), from which the escape into the ISM can be expected to occur about $50 - 100 \text{ kyr}$ after explosion on average (but see Bourguinat et al. 2025, for a revision).

The interaction of the pulsar with the ISM leads to the creation of a specific subclass of objects called bow-shock pulsar-wind nebulae (BSPWNe), in which the confinement of the nebula is now produced by the ram pressure of the medium crossed by the pulsar (Gaensler & Slane 2006; Bykov et al. 2017). High-resolution X-ray observations of the synchrotron emission from BSPWNe, especially thanks to the Chandra X-ray Observatory, have been key in revealing the nature of these objects and their astounding diversity (Kargaltsev et al. 2017). Valuable complementary information comes from measurements in the radio domain. GHz-emitting particles have long radiating lifetimes and should provide a time-integrated picture of the particle population. Moreover, their smaller Larmor radius make them sensitive to different acceleration and transport processes. Line observations in the optical and UV bands also turned out to be a relevant probe of BSPWNe in those cases where the pulsar moves through a partially ionized medium and collisional ionization or charge exchange can occur in the bow-shock head or tail.

About three dozens firm or candidate BSPWNe are known and there seems to be no two alike (Kargaltsev et al. 2017). They exhibit features as diverse as bipolar jets, torus-like components, bow-shaped shock fronts, long or short cometary tails, and one or two-sided misaligned coherent jets. The physical setup leading to the formation of all these structures, or specific combination thereof, remains unaccounted for. It potentially depends on a large number of parameters, intrinsic to the pulsar or related to the state of the ambient medium, and surely involves a multi-scale and multi-physics description, from AU-scale charged particle acceleration and transport to pc-scale supersonic and turbulent fluid dynamics. The recent discovery of extended gamma-ray halos around some of these objects put a new spin on the subject, although it is still unclear how common such a phenomenon is or whether it is connected to the pulsar itself or the ambient medium (López-Coto et al. 2022; Amato & Recchia 2024). Overall, BSPWNe are fascinating astrophysical setups providing insights into a rich variety of topics: structure of pulsar magnetospheres and pulsar wind nebulae; particle acceleration mechanisms in relativistic and turbulent flows; particle escape from a source, environmental conditions in the ISM, and early-stage non-thermal particle transport, with a connection to the question of local cosmic-ray leptons direct measurements.

Among BSPWNe, supersonically moving pulsars form a specific subset of neutron stars with kick velocities $\gtrsim 300 \text{ km s}^{-1}$, well above the sound speed in the different phases of the ISM at $3 - 30 \text{ km s}^{-1}$ (Kargaltsev et al. 2017). This configuration is expected to yield characteristic morphological patterns for the TS and CD (Bucciantini et al. 2005; Vigelius et al. 2007), as well as a relatively focused and extended tails. Prominent members of the class are: PSR B2224+65 and the Guitar nebula, PSR J1101–6101 and the Lighthouse nebula, PSR J2030+4415, PSR J1509–5850, and the recently discovered PSR J1638–4713 and the Potoroo nebula. Unambiguous identification of actual BSPWNe supersonically moving in the ISM is however challenging, and the distinction from younger PWNe still residing in their parent SNR and disrupted by a strongly asymmetric reverse shock is not obvious.

Interestingly, about half a dozen supersonic BSPWNe exhibit so-called misaligned filaments (Dinsmore & Romani 2024). These extend over parsec scales in the ISM with a linear and narrow morphology, in an oblique direction with respect to the pulsar proper motion. In a few cases, a weaker and shorter anti-filament is observed. They appear exclusively in X-rays and are thought to consist of synchrotron-emitting high-energy pairs escaping along ambient field lines from a specific location near the pulsar bow shock apex. A recent discussion of the theoretical challenges posed by these features, as well as an attempt to account for them from the process of non-resonant streaming instability, can be found in Olmi et al. (2024).

No radio counterpart of X-ray misaligned filaments have been observed so far, which suggests that the escape process might imply a threshold in energy that radio-emitting particles do not match. A common view on the phenomenon is that only the highest-energy pairs would be able to flow across the specific magnetic configuration formed by the bow-shock structure reconnecting to the ambient field on one side of the head, while lower-energy particles would be advected downstream. This fits in with the fact that BSPWNe tails have been observed in radio. The asymmetry and energy-dependent nature of particle escape in BSPWNe have been illustrated in simulations of BSPWNe (Barkov et al. 2019; Olmi & Bucciantini 2019b), and applied convincingly to some observations, e.g. PSR J2030+4415 (de Vries & Romani 2022).

Despite the non-detection of misaligned jets in radio (apart maybe from that reported in Khabibullin et al. 2024, in the Spaghetti nebula), it has been speculated that the population of long non-thermal filaments observed in the Galactic centre region would actually be the low-frequency analogues of misaligned X-ray jets. These radio filaments would be magnetic flux tubes currently illuminated after they happened to be connected to fast-moving pulsars in the recent past (Barkov & Lyutikov 2019). This scenario seems to be supported by X-ray observations of BSPWN candidate G0.13-0.11 ahead of an array of bright non-thermal filaments, with misaligned jets and a polarimetric signal matching expectations (Churazov et al. 2024). Non-thermal radio filaments are a valuable setup to study particle transport processes at GeV particle energies, where most of the cosmic-ray power lies (Thomas et al. 2020).

In this paper, we focus on MeerKAT radio observations of a large region encompassing PSR J1101–6101 and the Lighthouse nebula, together with the SNR MSH 11-61A. The Lighthouse nebula was originally detected as hard X-ray source IGR J11014-6103, located southwest of the SNR MSH 11-61A, and exhibits a complex morphology in X-rays comprising a point source, an elongated cometary tail, a prominent one-sided jet-like feature perpendicular to it, and a weaker and smaller counter-jet (Pavan et al. 2011, 2014, 2016). The PWN nature of the system was confirmed by the detection of PSR J1101–6101, with a period $P = 62.8 \text{ ms}$, a spin-down power of $L = 1.36 \times 10^{36} \text{ erg s}^{-1}$ and a spin-down time scale of 116 kyr (Halpern et al. 2014). The orientation of the nebula points back towards the centre of SNR MSH 11-61A, which suggests it is the parent remnant to the pulsar. The whole system lies at an estimated distance $7 \pm 1 \text{ kpc}$ (Reynoso et al. 2006), and has a possible age of about 20 kyr that implies a projected kick velocity of about 1000 km s^{-1} for the pulsar. The Lighthouse nebula sports the brightest, longest, and most distant X-ray jet among those known so far, with a length of about 10 pc (Dinsmore & Romani 2024). The misaligned jets and the pulsar were not detected at radio wavelengths but the tail of the nebula clearly shows up in 2 GHz ATCA observations (Pavan et al. 2014).

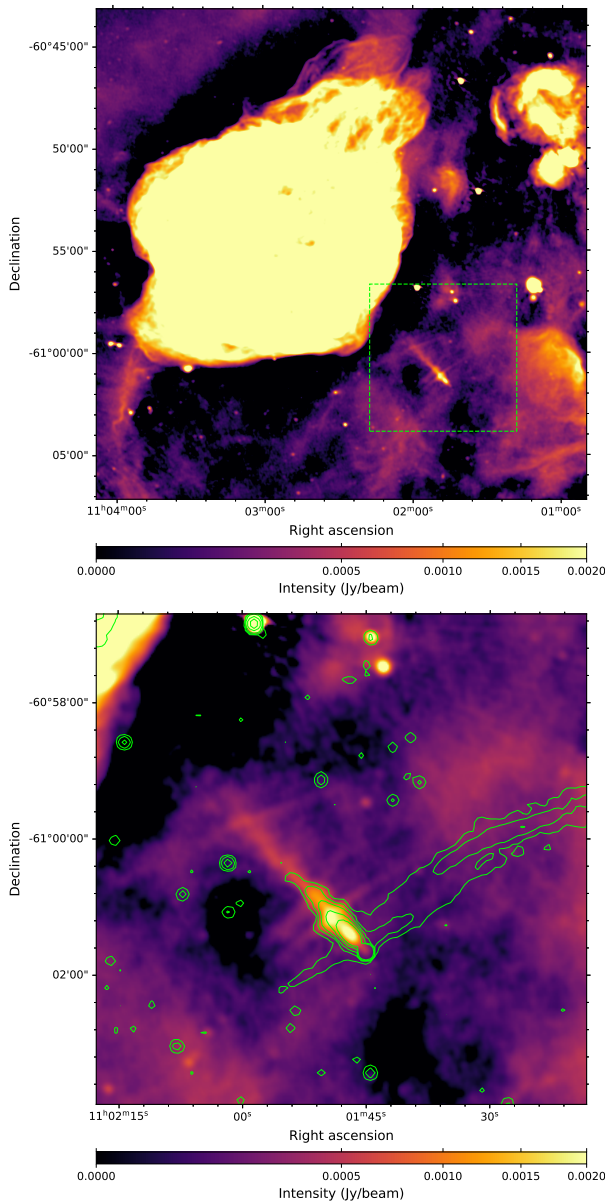


Fig. 1: Intensity map of the central part of the region covered by our MeerKAT observations. The top panel displays a broad view dominated by a large and saturated source which is SNR MSH 11-61A. The bottom panel is a zoom on the Lighthouse Nebula. The green contours correspond to the X-ray photon flux measured with Chandra/ACIS in the 0.5 – 7 keV band.

2. MeerKAT observations

2.1. Data taking and processing

We observed the field of PSR J1101–6101 with the MeerKAT radio telescope (Jonas & MeerKAT Team 2016) at L-band (856–1712 MHz) over two epochs. The first observation took place on March 16 2021 with 63 antennas and a total integration time of 4.2 hours, while the second was conducted on June 1 2021 with 59 antennas for 3.7 hours, yielding a combined on-source time of 6.3 hours. Both observations used the 4k wideband continuum mode, providing 4096 frequency channels across the band. The primary calibrator J0408–6545 was observed at the start and end of each session for flux density and bandpass calibration, while the secondary calibrator J0906–6829 was visited at reg-

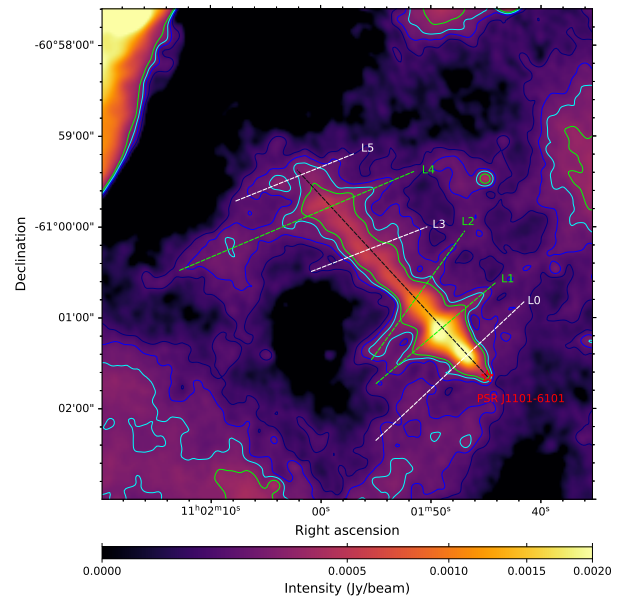


Fig. 2: Intensity map of a zoomed-in region centred on the Lighthouse Nebula. The position of PSR J1101-6101 is marked as a red star, and the contours correspond to emission at a significance of 3, 5, 7, and 10 σ . The black dashed line gives the longitudinal axis of the nebula, the green and white dashed lines indicate conspicuous and tentative transverse emission streaks, respectively.

ular intervals for time-dependent gain corrections. Data reduction followed standard procedures using the CARACAL pipeline (Józsa et al. 2020). The calibrated measurement sets from both epochs were combined and imaged using WSCLEAN (Offringa et al. 2014) with Briggs weighting (robust = 0), applying multi-scale and multi-frequency synthesis deconvolution. The final image achieves a RMS noise of $30\mu\text{Jy beam}^{-1}$ near the phase centre, with a synthesised beam of $7.7'' \times 6.9''$ at a position angle of 60.5° .

2.2. Intensity maps

Figure 1 displays the radio intensity distribution over the entire field and within a smaller region around the Lighthouse Nebula. MeerKAT reveals highly structured radio emission including new features. The Lighthouse Nebula sports an extended ~ 6 pc radio tail, which was partly detected already from ATCA observations (Pavan et al. 2014). Besides providing a broader picture of that component, MeerKAT unveiled an array of streaks/filaments transverse to the tail. Three are obvious and are marked in green in Fig. 2 (and labeled L1, L2, and L4), while three are more tentative and are marked in white (and labeled L0, L3, and L5). We provide in Table 1 the distance from the pulsar (position of the intersection of the black and green or white lines in Fig. 2) and the length of each streak (decomposed into its northern and southern parts).

The top panel of Fig. 4 displays intensity profiles over three lines along the tail: one line starting from the pulsar and running through the source until the end of the (detectable) tail, and two parallel lines shifted by 12 arcmin in the northwestern and southeastern directions and probing intensity on the sides of the tail, where the streaks connect. The latter allow us to visualize in a different way the reality of the streaks by showing clear intensity

Table 1: Angular position and extent of the radio streaks

	Distance from pulsar	Length (North+South)
L0	19.6"	51"+1.4'
L1	44.1"	45"+59"
L2	1.17'	54"+51"
L3	1.90'	39"+42"
L4	2.54'	1.8"+58"
L5	3.02'	35"+49"

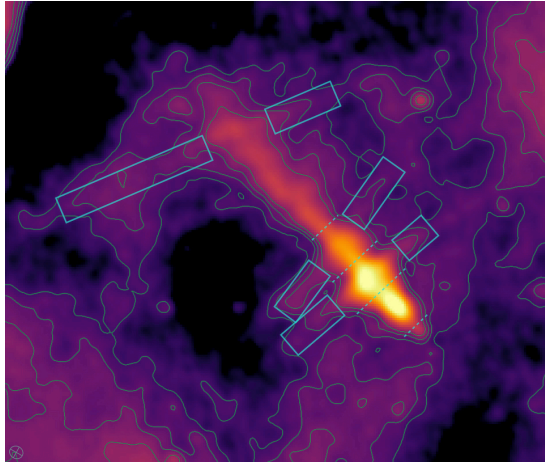


Fig. 3: Chart illustrating the regions used for flux and spectral index extraction. The blue boxes correspond to the north and south parts of the main streaks L1, L2, and L4. The blue dashed lines separate the tail into five regions: pulsar, head, shoulder, hip, and leg (from bottom-right to top-left).

enhancements at around 0.7, 1.1, and 2.7 arcmin from the pulsar, corresponding respectively to L1, L2, and L4. The tentative streaks L0, L3, and L5 appear as more modest signal increases at 0.3, 1.7, and 3.1 arcmin.

The bottom panel of Fig. 4 displays intensity profiles along the main streaks L1, L2, and L4. Positions were rescaled to have peak intensity at zero, with positive distances corresponding to the southeast direction. The plot illustrates the very similar intensities in all three streaks, on either side of the tail, despite their different distances from the pulsar.

The flux from selected regions in the source are listed in Table 2 together with their uncertainties (see Fig. 3 for a chart of the different regions). The latter were estimated as the average standard deviation of the residual signal over the region footprint within adjacent source-free areas. In the longitudinal tail, they were extracted within the 10σ contour and for four different regions: one for each emission maximum downstream of the pulsar, and one for the remainder of the tail. In addition, we extracted the flux density of the weak emission spot coincident with the pulsar. In the main transverse streaks, we extracted the flux in rectangular regions of 15 arcmin width starting at the 10σ contour and capturing roughly the $> 3\sigma$ flux. The values are given in Table 2 as the sum of two terms: the flux on the southeastern and northwestern sides of the longitudinal tail, respectively. The total flux in each streak is in the range $\sim 3 - 6$ mJy, meaning the total flux in all 3+3 streaks is comparable with that of the brightest part of the tail.

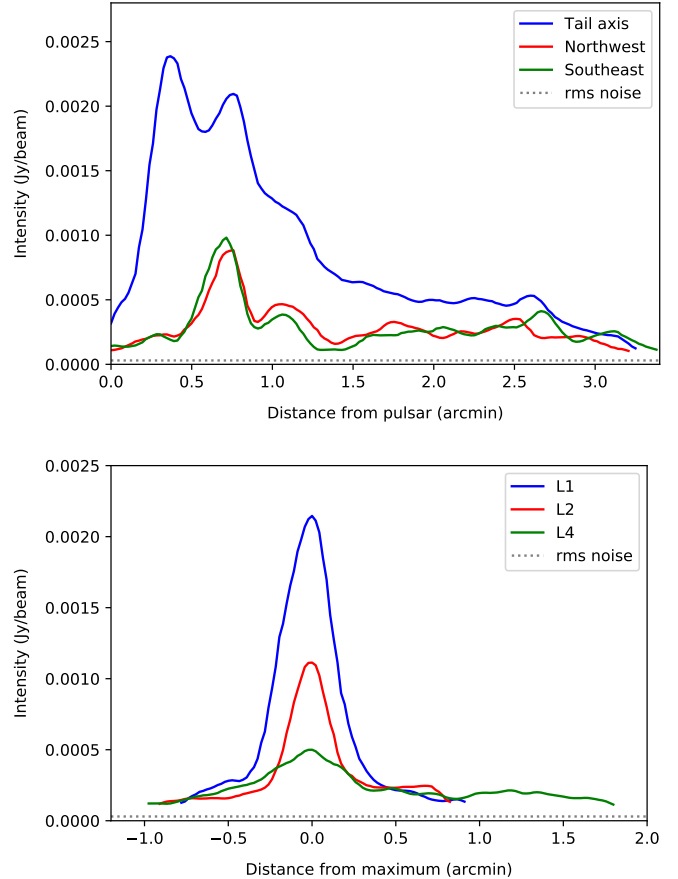


Fig. 4: Radio intensity profiles of the Lighthouse Nebula. The top panel displays the intensity in the longitudinal direction along the tail, for the central axis and along two directions shifted sideways in the northwestern and southeastern directions. The bottom panel displays the intensity along the three main streaks.

2.3. Spectral index

To produce a spectral index map, we split the full L-band bandwidth into two sub-bands. Each sub-band was imaged independently using the same WSCLEAN parameters as for the full-band image. The CASA task `immath` (CASA Team et al. 2022) was then used to compute the spectral index α (defined as $S_\nu \propto \nu^\alpha$) on a pixel-by-pixel basis. Only pixels with flux densities exceeding 5σ in both sub-band images were used.

We extracted the average spectral index over the same selected regions as in Sect. 2.2 and reported the values in Table 2. Because of the weak intensity of the source and the fact that we could rely only on observations in one band, the estimated spectral indices are relatively uncertain. In Table 2, the average spectral index for each region is provided together with the mean uncertainty on individual pixel values and with the standard deviation of spectral index values over the region. The first quantity is seen as representative of the statistical uncertainty, while the second quantity is a measure of the systematic uncertainty. It can be seen that, as surface brightness decreases (from head to leg), both uncertainties increase, especially the systematic one. Eventually, this attempt to estimate the spectral index confirms that the value in the brightest part, the head, is consistent with typical values found in other similar objects, ranging from -0.4 to

Table 2: Flux and spectral index for selected regions

Region	Flux density (mJy)	Spectral index
Pulsar	0.42 ± 0.05	-
Head	10.8 ± 0.4	$-0.4 \pm 0.2 \pm 0.4$
Shoulder	14.3 ± 0.5	$-0.1 \pm 0.2 \pm 1.1$
Hip	8.1 ± 0.4	$0.4 \pm 0.2 \pm 1.1$
Leg	14.8 ± 1.1	$2.1 \pm 0.5 \pm 1.4$
L1	$(1.3 \pm 0.3) + (1.0 \pm 0.2)$	-
L2	$(1.6 \pm 0.3) + (1.5 \pm 0.3)$	-
L4	$(3.9 \pm 0.7) + (1.6 \pm 0.3)$	-

0.0 (for instance -0.21 in Potoroo and -0.16 for the Goat's Eye; see Lazarević et al. 2024; Ghavam et al. 2025).

2.4. Summary of observables

From the processed MeerKAT data, both intensity map and spectral index estimates, we could make a number of observations.

The tail can be decomposed into two parts: the brightest section extending ~ 2.5 pc from the pulsar, and a dimmer portion further out. The bright part exhibits the following properties:

1. A faint emission at the pulsar position and over about 0.5 pc downstream of it in the north-east direction
2. A strong rise in emission leading to a maximum, followed by a dip and a second maximum, a rapid decrease of the emission until a third maximum or plateau, with a separation between maxima of about 1 pc and of the order of the lateral extent of the tail
3. A spectral index at 0.9–1.6 GHz broadly in the range -0.8 to 0.0, typical of synchrotron emission from BSPWNe.

The first maximum in radio emission matches the peak in X-ray 0.5 – 10 keV emission (Pavan et al. 2014, ; see also the bottom panel of Fig. 1).

At larger distances from the pulsar, the second and dimmer part of the tail is characterized by:

1. A progressive decrease in intensity over 3.5 pc
2. Some wobbling around the longitudinal axis

The wobbling about the longitudinal axis is reminiscent of the zig-zag behaviour observed in the PWN inside SNR N206 in the Large Magellanic Cloud (Ghavam et al. 2025).

The newly detected streaks/filaments transverse to the tail have the following properties:

1. Some coincide with brightening parts of the tail (L0, L1, and L2) and one corresponds to a lateral broadening (L1)
2. They appear on both sides with similar lengths and with an apparent continuity from one side to the other
3. They do not correspond to the known X-ray jet and counter-jet system and no streak emerges from the bow-shock apex
4. The separation between streaks along the tail is similar to the lateral extent of the tail (~ 1 pc)
5. No striking evolution of the intensity, length, or width of the streaks along the pulsar trajectory

The coincidence between the lateral streaks and emission maxima along the tail suggests that these faint features are not spurious artefacts introduced in the data reduction.

3. Interpretation

3.1. Can radio streaks be the counterparts of X-ray jets ?

A natural interpretation for the radio structures would be that of a relic trace of the same feature that we observe in X-rays close to the PSR. Nevertheless this picture can be readily ruled out. If radio emission from the streaks comes from the same particles originally emitting in the X-rays, this means that in the time needed for the PSR to move from a streak to its present position, the particles must have lost enough energy to now be able to emit photons in the radio band. In the $\sim 30 \mu\text{G}$ amplified magnetic field (δB) of the X-ray feature (Pavan et al. 2014; Olmi et al. 2024), this means a decrease in particle energy from 40 – 100 TeV to 3-4 GeV. But this requires a much longer time than the travel time between any of the streaks and the current pulsar position. Considering the first streak, L1, this travel time is $t_{\text{X-L1}} \simeq 1780 - 590$ yr, where the interval is set by the range of possible values for the PSR speed ($V_{\text{PSR}} = 800 - 2400$ km/s). The most favorable scenario to make an interpretation of the radio streaks as relics of the X-ray features viable is one in which the amplified magnetic field δB_X survives for $t_{\text{X-L1}}$ before eventually dropping to the ISM value $B_{\text{ISM}} = 3 \mu\text{G}$. The 40 – 100 TeV particles, originally emitting X-ray photons in δB_X , will now produce UV light, to which we are almost blind due to ISM absorption, both in the amplified field and in the ambient one. In fact, one can expect the amplified magnetic field to start decaying as soon as the pulsar moves away and the injection of particles in the flux tube stops. In this case the synchrotron loss-time becomes even longer, and particles originally emitting in X-rays would still emit X-rays, but at a level difficult to detect over the background noise ($\text{S/N} \sim 3$ at best).

Along the same lines, one might think that radio emitting particles were already present in the original X-ray feature, that becomes a radio feature as soon as the magnetic field decays enough to prevent any X-ray emission. On the one hand, it is difficult to explain how to extract low energy particles efficiently from the bow shock apex to populate the filament, given their much smaller Larmor radii ($10^{-4} - 10^{-5}$) compared to the X-ray emitting particles (Olmi & Bucciantini 2019b). On the other hand, even if this were the case, we might expect to detect radio emission from the X-ray feature as well. We will quantify this statement in the following section. It becomes then apparent that the nature of the particles responsible for these two kinds of structures (X-ray filament and radio streaks) is different.

3.2. Synchrotron-emitting particle populations in the system

A relevant piece of information comes from the measured spectral indices (radio and X-rays) in the PWN (see the previous Sec. 2.3 and Pavan et al. 2016) and in the X-ray feature (Pavan et al. 2016; Klingler et al. 2023). In general the emission spectrum of a PWN is well accounted for by assuming the injection of two different particle populations, both described as power-law spectral distributions, but with different spectral indices below and above some Lorentz factor γ_B , namely: $f(\gamma, t) = N_0(t)(\gamma/\gamma_B)^{-p_i}$, where $p_i \equiv p_L$ for $\gamma \leq \gamma_B$, while $p_i \equiv p_H$ for $\gamma > \gamma_B$. The spectral index of synchrotron radiation α (now defined as $S_\nu \propto \nu^{-\alpha}$) is related to that of the emitting particle distribution q as $\alpha = (q - 1)/2$; q is in turn related to the injection spectral index as $q = p$ at low enough energy, where synchrotron losses are not severe ($\gamma < \gamma_s$), and $q = p+1$ for particles that radiate effectively ($\gamma > \gamma_s$), with γ_s the Lorentz factor corresponding to the synchrotron cooling break. The spectral analysis of a num-

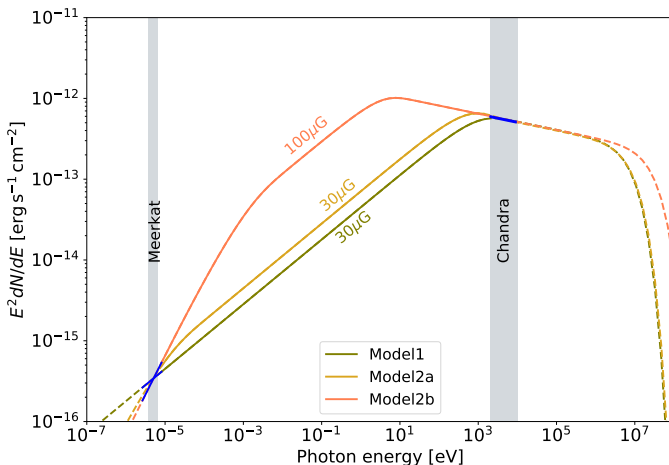


Fig. 5: Spectral energy distribution function (SED) computed using different models for the particle injection spectrum: Model1 assumes a single particle population (and a radiation spectral index $\alpha = 0.6$); Model2a/b assume two populations (radiation spectral indices $\alpha_L = 0.0$ and $\alpha_H = 0.6$), with a different position of the intrinsic and synchrotron break (γ_b and γ_s) depending on the nebular magnetic field strength. The nebular magnetic field of each case is reported on the plot, with the same color coding as the curve it refers to. Observational bands are shown as gray shaded regions. Blue segments identify the spectral slopes in the observed windows.

ber of PWNe indicates $\gamma_B \sim 10^5 - 10^6$ (e.g. Bucciantini et al. 2011; Torres et al. 2014) and $\alpha_{\text{low}} \sim 0 - 0.3$, while $\alpha_{\text{high}} \sim 0.6$.

It is peculiar that in the case of the Lighthouse PWN, the measured photon index ($\Gamma = \alpha + 1$) is $\Gamma_X \simeq 1.7 - 2.5$ (see Fig. 6 in Pavan et al. 2016) up to a distance of $\sim 50''$ from the pulsar, which is approximately where the first bright part of the tail (in between L1 and L2) terminates. The photon index then softens with increasing distance from the pulsar, suggesting synchrotron cooling along the main tail. The average value in that region is $\Gamma_X \sim 2.1$ in terms of photon index, implying a spectral index $\alpha_X \sim 1.1$, compatible with a cooled spectrum.

On the other hand, the radio spectral index extracted from the PWN varies between 0.0 and 0.8 (see Table 2), and further downstream it could be much steeper than in other similar sources (e.g. Lazarević et al. 2024). This suggests two possible interpretations of the observed spectrum: i) a standard description with two particle populations including a flat low energy component ($\alpha_L = 0.0$); ii) a spectrum described by a single population with $\alpha \simeq 0.6$. In this second case, if a flat spectrum low energy population exists, the intrinsic break must be below few $\times 10^3$ (corresponding to $\sim \text{GeV}$), so that this component does not show in the emission spectrum. In both cases a synchrotron break (γ_s) must occur between the Meerkat and Chandra observational bands, to allow for a 1/2 steepening of the spectral index due to radiation cooling, leading to a cooled value of $\alpha \simeq 1.1$.

The situation is different for the X-ray feature, where the measured photon index is compatible with the un-cooled one: $\Gamma_X \sim 1.3 - 1.8$ in the first $150''$ from the pulsar. This matches the expectation that the particles populating the X-ray feature escape the BSPWN before starting to cool in the PWN and that in the feature we are observing their injection spectrum (Olmi & Bucciantini 2019b).

Considering the particle spectral models discussed above, we have produced different possible PWN spectra¹ to fit the available data (Meerkat and Chandra bands). Fixing the observational energies and detected fluxes and taking into account the large range of possible values for the PSR velocity (800-2400 km/s) due to the association with a nearby young SNR (García et al. 2012), we have determined the magnetic field in the PWN, the injection break γ_B and synchrotron break γ_s for each scenario. Our results are summarized in Fig. 5 (Model1 for a single particle population, Model2 for two populations at injection). We limited the possible models to cases consistent with a magnetic field below $\sim 100 \mu\text{G}$. Additionally we found that no fit to the data is possible assuming $\alpha > 0.6$.

Of course this is a simplified description based on a one-zone modeling that can only catch the average magnetic field needed to reproduce the observed fluxes. The considered magnetic field strengths are not too far from the equipartition value $\sim 40 \mu\text{G}$ that we estimate, based on the expression by Pacholczyk (1970), both from radio and X-ray emission.

An important check on the reliability of this picture requires the computation of: i) the fraction of energy that goes into illuminating the system compared with the available energy injected by the pulsar; ii) the number of particles needed to feed the PWN and the features.

The energy injected by the pulsar in each region of the system within a distance Δd from the pulsar can be roughly estimated as: $E_{\text{inj}} \sim \dot{E} \Delta d / V_{\text{PWN}}$. For example, the energy injected in the main (brighter) part of the PWN, within a distance $\Delta d \simeq d_1$, corresponding to the distance between the pulsar and L1 $\simeq 1.5$ pc, is: $E_{\text{inj},1} \sim 4 \times 10^{46}$ erg. On the other hand, the energy needed to power each region of the system can be obtained by integration of the magnetic field and particle energy density derived from fitting the emission. What we found playing this game is that a fraction $\sim 20\%$ of the available energy goes into accelerated particles, a number compatible with what expected for PWNe; for the Crab Nebula for example, a fraction of $\sim 30\%$ was estimated (Hester 2008). A fraction of $\sim 40\%$ is required to power the entire system, considering the main PWN region, up to distance d_1 , the first streak and the X-ray feature.

The number of particles injected in each part of the system (PWN/feature/streaks), N , can be directly computed from the normalization of the injection spectrum, fixed by the comparison with observed fluxes in the different regions. Depending on the spectral model and assumed V_{PSR} , we find different numbers, in the range $N \simeq 2 \times 10^{47} - 6 \times 10^{48}$ particles. From this, one obtains the particle injection rate: $\dot{N} = N V_{\text{PSR}} / \Delta d$. Then comparing with the theoretical pair production rate $\dot{N}_{\text{GJ}} = (2\pi/P)^2 B_* R_*^3 / (ec)$ (Goldreich & Julian 1969), with P the pulsar period, B_* the magnetic field at the star surface and $R_* \sim 10$ km the pulsar radius, allows an estimate of the pulsar pair multiplicity (κ) required to support our interpretation. We obtain $\kappa \simeq \dot{N} / \dot{N}_{\text{GJ}} \sim 10^4 - 10^6$, with the extreme of the interval corresponding to the most extreme cases under consideration: $V_{\text{PSR}} = 800$ km/s, and an injection spectrum with two populations implying an ambient field of $\sim 100 \mu\text{G}$; or $V_{\text{PSR}} = 2400$ km/s, and an injection spectrum with a single population. These estimates are in the range of theoretical expectations (see e.g. the discussion in Amato 2014, and references therein), and centered around the value that modeling of well studied PWNe indicates as average Bucciantini et al. (2011); Torres et al. (2014).

¹ Synchrotron spectral models have been produced using the NAIMA python library (Zabalza 2015).

3.3. Possible physical origin for the radio streaks

In our interpretation, the most realistic origin of the radio streaks is that of dynamically-induced features. The tail of a BSPWN is expected to become dynamically unstable at a certain distance from the pulsar (Olmi & Bucciantini 2019a). Moreover, the shape of the main PWN region (up to distance $\sim d_1$) is reminiscent of what is observed in other systems, such as the Guitar nebula (Cordes et al. 1993). The widening of the tail at the shoulders can be interpreted as the effect of the mass loading of neutral atoms from the ambient (Morlino et al. 2015). This not only produces a modification of the tail shape, but also favors the formation of instabilities (Olmi et al. 2018). Unfortunately, it is impossible to constrain the mass-loading in the Lighthouse nebula, given that only an upper limit exists on $\text{H}\alpha$ emission, $F_{\text{H}\alpha} \lesssim 1.3 \times 10^{-17} \text{ erg/s/cm}^2/\text{arcsec}^2$ (Pavan et al. 2016), and this is compatible with any neutral fraction.

As soon as the tail structure breaks up due to instabilities, one can anticipate a massive injection of particles into the ambient medium. In this dynamically-driven proposed scenario, all the particles present in the tail are expected to escape with the same probability, conversely to what happens into the X-ray feature. Then one needs to account for the non-detection of the streaks in X-rays. However, the expected X-ray flux in each streak, computed using the same description for the spectrum as discussed in Sect. 3.2, is at the level of the background noise in the Chandra data. Moreover, in this case no charge separation of the escaping particles is expected, in contrast with the reconnection-driven escape at the base of the X-ray feature. This is a relevant point, since radio streaks appear double sided, with almost the same extension of the two parts, different from the X-ray features, which is characterized by a strong asymmetry connected with the charge-separated escape (Olmi & Bucciantini 2019b).

Once escaped, the particles interact with the ambient magnetic field. The longitudinal extension (l_i) of the streaks cannot be interpreted as an effect of synchrotron cooling: the needed magnetic field for such an interpretation is of order tens of mG, which is not realistic. If particle propagation is governed by diffusion, then one can relate l_i to the local diffusion coefficient D as: $l_i \simeq \sqrt{D\Delta t_i}$, where the characteristic time involved here can be assumed to be the time required for the pulsar to travel a distance d_i ($\Delta t_i = d_i/V_{\text{PSR}}$). From the previous relation we estimate: $D \simeq 2 - 6 \times 10^{27} \text{ cm}^2 \text{ s}^{-1}$, for $\Delta t_1 = d_1/V_{\text{PSR}}$; this is an order of magnitude lower than the standard Galactic diffusion coefficient at the energy of the emitting particles, and it implies a perturbation of the magnetic field by $\delta B/B \simeq \sqrt{cR_L(E_{\text{MeerKAT}})/(3D)} \sim 10^{-3} - 10^{-2}$ on a scale $R_L(E_{\text{MeerKAT}})$, corresponding to the Larmor radius of the particles emitting in the MeerKAT energy band. From the diffusion of cosmic rays in the Galaxy (Evoli et al. 2021) we estimate a diffusion coefficient on the scale of interest $R_L(E_{\text{MeerKAT}})$ of $D_{\text{Gal}} = 7.9 \times 10^{28} \text{ cm}^2 \text{ s}^{-1}$, corresponding to an expected turbulence level of $\delta B/B \simeq 10^{-3}$, which is compatible with the required one. It is then not unrealistic that normal ISM turbulence alone is responsible for the local modification of the magnetic field required to explain the extension of the radio features.

Given the relatively small value inferred for the diffusion coefficient in the streaks, another possibility is that the escaping particles produced their own turbulence via some self-generated instability, in particular the resonant streaming instability. Since the radio features are thought to be produced by escaping particles that are not charge-separated, there is no net current to excite the non-resonant one (as theorized for the X-ray feature), although see Orusa & Sironi (2025). The data at our disposal do

not permit to investigate this scenario in detail yet, but a better characterization of the newly detected streaks from future deeper radio observations may allow us to go further. More accurate intensity profiles and spectral index information along the streaks could be checked against estimates for the growth and damping rate of the streaming instability, thereby providing an interesting test bench for fundamental processes of cosmic-ray transport (in the same spirit as Thomas et al. 2020, on synchrotron harps at the Galactic Center).

4. Summary and conclusion

In this work, we presented the analysis of radio observations of the Lighthouse Nebula with MeerKAT. The good sensitivity of MeerKAT on intermediate angular scales revealed highly structured emission from the system and allowed us to expand our view on the development of the synchrotron nebula downstream of the bow shock of fast-moving pulsar PSR J1101-6101. For the first time, we detect the extension of the tail up to beyond 5pc from the pulsar in the opposite direction to its proper motion, and a system of multiple transverse two-sided emission streaks qualitatively reminiscent of some phenomena observed in the vicinity of the Galactic Centre region (non-thermal filaments and synchrotron harps). Conversely, no radio counterpart of the long misaligned X-ray jet sported by the Lighthouse Nebula is seen, suggesting different physical origins for the X-ray and radio features.

The radio to X-ray emission from the tail can be accounted for from a particle population energized close to the pulsar and progressively cooling as it is advected downstream, producing synchrotron emission in a $30 - 100 \mu\text{G}$ magnetic field. The observed broadband synchrotron emission requires about 20–40% of the pulsar spin-down power to be converted into relativistic leptons and involves pair multiplicity in the $10^4 - 10^6$ range, in agreement with theoretical expectations and observations of other pulsars.

The transverse radio streaks are interpreted as the occasional release of leptons from the tail into the surrounding medium. The release could be triggered by dynamical instabilities of the flow in the tail, which would break the confinement of particles and allow them to propagate in the ambient medium. The fact that we observe brightening and/or broadening of the tail at the base of the streaks lends support to that scenario and indeed suggests significant reorganization of the flow. In the Lighthouse Nebula, the observed intensities along the tail and in the streaks suggests that most of the particle content is discharged in the environment within 2–3 pc (a non-exclusive interpretation is that the magnetic field in the tail undergoes a significant decay). Once set free, particles light up the ambient magnetic field and, in the present case, they reveal a magnetic field with a coherence length of at least a few parsec. The length and persistence of the streaks imply a degree of magnetic turbulence that is consistent with, or slightly enhanced compared to, the galactic average at the relevant scales, as estimated based on large-scale cosmic-ray transport models. The observed intensity in the streaks does not necessarily call for strong enhancements of the total magnetic field strength but it is compatible with a higher than average ($3 \mu\text{G}$) ISM magnetic field.

We encourage deep radio observations of this and similar BSPWN systems in order to improve our understanding of non-thermal particle transport in these complex objects. A better appraisal of particle escape from pulsar-powered sources is of great importance for many topics such as the characterization of magnetic turbulence and transport conditions in the vicinity of

cosmic-ray accelerators, the identification of the specific mechanisms leading to the formation of pulsar gamma-ray halos, and the interpretation of the local cosmic-ray positron flux.

Acknowledgements. Pierrick Martin, Mickael Coriat, and Alexandre Marcowith acknowledge financial support by ANR through the GAMALO project under reference ANR-19-CE31-0014. Barbara Olmi, Elena Amato, Niccolò Bucciantini and Sarah Recchia acknowledge financial support by the European Union – NextGenerationEU RRF M4C2 1.1 grant PRIN-MUR 2022TJW4EJ. This work has made use of the SIMBAD database, operated at CDS, Strasbourg, France, and of NASA's Astrophysics Data System Bibliographic Services. The preparation of the figures has made use of the following open-access software tools: Astropy (Astropy Collaboration et al. 2013), Matplotlib (Hunter 2007), NumPy (van der Walt et al. 2011), SciPy (Virtanen et al. 2020), and Naima (Zabalza 2015). The MeerKAT data published here have been reduced using the CARACal pipeline, partially supported by ERC Starting grant number 679627 FORNAX, MAECI Grant Number ZA18GR02, DST-NRF Grant Number 113121 as part of the ISARP Joint Research Scheme, and BMBF project 05A17PC2 for MeerKAT. Information about CARACal can be obtained online under the URL: <https://caracal.readthedocs.io>

References

Amato, E. 2014, in International Journal of Modern Physics Conference Series, Vol. 28, International Journal of Modern Physics Conference Series, 1460160

Amato, E. & Recchia, S. 2024, Nuovo Cimento Rivista Serie, 47, 399

Astropy Collaboration, Robitaille, T. P., Tollerud, E. J., et al. 2013, A&A, 558, A33

Bandiera, R., Bucciantini, N., Olmi, B., & Torres, D. F. 2023, MNRAS, 525, 2839

Barkov, M. V. & Lyutikov, M. 2019, MNRAS, 489, L28

Barkov, M. V., Lyutikov, M., Klingler, N., & Bordas, P. 2019, MNRAS, 485, 2041

Bourguinat, L.-M., Evoli, C., Martin, P., & Recchia, S. 2025, Accepted for publication in A&A, arXiv:2507.01495

Bucciantini, N., Amato, E., & Del Zanna, L. 2005, A&A, 434, 189

Bucciantini, N., Arons, J., & Amato, E. 2011, MNRAS, 410, 381

Bykov, A. M., Amato, E., Petrov, A. E., Krassilchtkhikov, A. M., & Levenfish, K. P. 2017, Space Sci. Rev., 207, 235

CASA Team, Bean, B., Bhatnagar, S., et al. 2022, PASP, 134, 114501

Churazov, E., Khabibullin, I., Barnouin, T., et al. 2024, A&A, 686, A14

Cordes, J. M., Romani, R. W., & Lundgren, S. C. 1993, Nature, 362, 133

de Vries, M. & Romani, R. W. 2022, ApJ, 928, 39

Dinsmore, J. T. & Romani, R. W. 2024, ApJ, 976, 4

Evoli, C., Amato, E., Blasi, P., & Aloisio, R. 2021, Phys. Rev. D, 103, 083010

Gaensler, B. M. & Slane, P. O. 2006, ARA&A, 44, 17

García, F., Combi, J. A., Albacete-Colombo, J. F., et al. 2012, A&A, 546, A91

Ghavam, M., Smeaton, Z. J., Filipovic, M. D., et al. 2025, arXiv e-prints, arXiv:2512.01221

Goldreich, P. & Julian, W. H. 1969, ApJ, 157, 869

Halpern, J. P., Tomsick, J. A., Gotthelf, E. V., et al. 2014, ApJ, 795, L27

Hester, J. J. 2008, ARA&A, 46, 127

Hunter, J. D. 2007, Computing in Science Engineering, 9, 90

Igoshev, A. P. 2020, MNRAS, 494, 3663

Jonas, J. & MeerKAT Team. 2016, in PoS, Vol. MeerKAT2016, MeerKAT Science: On the Pathway to the SKA, 001

Józsa, G. I. G., White, S. V., Thorat, K., et al. 2020, in ASP Conf. Ser., Vol. 527, ADASS XXIX, ed. R. Pizzo, E. Deul, J.-D. Mol, J. de Plaa, & H. Verkouter, San Francisco, 635–638

Kargaltsev, O., Pavlov, G. G., Klingler, N., & Rangelov, B. 2017, Journal of Plasma Physics, 83, 635830501

Khabibullin, I. I., Churazov, E. M., Bykov, A. M., Chugai, N. N., & Zinchenko, I. I. 2024, MNRAS, 527, 5683

Klingler, N., Hare, J., Kargaltsev, O., Pavlov, G. G., & Tomsick, J. 2023, ApJ, 950, 177

Lazarević, S., Filipović, M. D., Dai, S., et al. 2024, PASA, 41, e032

López-Coto, R., de Oña Wilhelmi, E., Aharonian, F., Amato, E., & Hinton, J. 2022, Nature Astronomy, 6, 199

Mitchell, A. M. W. & Gelfand, J. 2022, in Handbook of X-ray and Gamma-ray Astrophysics, ed. C. Bambi & A. Sangangelo, 61

Morlino, G., Lyutikov, M., & Vorster, M. 2015, MNRAS, 454, 3886

Offringa, A. R., McKinley, B., Hurley-Walker, N., & others. 2014, MNRAS, 444, 606

Olmi, B. 2023, Universe, 9, 402

Olmi, B., Amato, E., Bandiera, R., & Blasi, P. 2024, A&A, 684, L1

Olmi, B. & Bucciantini, N. 2019a, MNRAS, 484, 5755

Olmi, B. & Bucciantini, N. 2019b, MNRAS, 490, 3608

Olmi, B. & Bucciantini, N. 2023, PASA, 40, e007

Olmi, B., Bucciantini, N., & Morlino, G. 2018, MNRAS, 481, 3394

Orusa, L. & Sironi, L. 2025, arXiv e-prints, arXiv:2512.15847

Pacholczyk, A. G. 1970, Radio astrophysics. Nonthermal processes in galactic and extragalactic sources

Pavan, L., Bordas, P., Pühlhofer, G., et al. 2014, A&A, 562, A122

Pavan, L., Bozzo, E., Pühlhofer, G., et al. 2011, A&A, 533, A74

Pavan, L., Pühlhofer, G., Bordas, P., et al. 2016, A&A, 591, A91

Reynoso, E. M., Johnston, S., Green, A. J., & Koribalski, B. S. 2006, MNRAS, 369, 416

Thomas, T., Pfrommer, C., & Enßlin, T. 2020, ApJ, 890, L18

Torres, D. F., Cillis, A., Martín, J., & de Oña Wilhelmi, E. 2014, Journal of High Energy Astrophysics, 1, 31

van der Swaluw, E., Achterberg, A., Gallant, Y. A., & Tóth, G. 2001, A&A, 380, 309

van der Walt, S., Colbert, S. C., & Varoquaux, G. 2011, Computing in Science Engineering, 13, 22

Verbunt, F., Igoshev, A., & Cator, E. 2017, A&A, 608, A57

Viglius, M., Melatos, A., Chatterjee, S., Gaensler, B. M., & Ghavamian, P. 2007, MNRAS, 374, 793

Virtanen, P., Gommers, R., Oliphant, T. E., et al. 2020, Nature Methods, 17, 261

Zabalza, V. 2015, in International Cosmic Ray Conference, Vol. 34, 34th International Cosmic Ray Conference (ICRC2015), 922